ADVANCED MATERIALS INTERFACES
Open Access
www.advmatinterfaces.de

$LiNbO_3$ Coatings on NCM622: Structure and Performance Insights

*Johannes Haust, Yiran Guo, Jürgen Belz, Shamail Ahmed, Narges Adeli, Franziska Hüppe, Linus C. Erhard, Valeriu Mereacre, Jochen Rohrer, Anna-Lena Hansen, Helmut Ehrenberg, Karsten Albe, Joachim R. Binder, and Kerstin Volz**

For enhancing the electrochemical performance of solid-state batteries (SSBs), protective coatings are applied on the cathode active material (CAM) to mitigate the degradation of the cathode/electrolyte interface. A comprehensive understanding of the structural properties of these coatings is crucial for further optimization. This study investigates the effect of $LiNbO_3$-related coatings on $LiNi_{0.6}Co_{0.2}Mn_{0.2}O_2$ (NCM622) CAM, focusing on the relationship between coating structure and electrochemical performance in battery cells. Therefore, three samples calcinated at 550, 350 and, 80 °C temperature are analyzed with scanning transmission electron microscopy (STEM), energy dispersive X-ray spectroscopy (EDS), and scanning precession electron diffraction (SPED) in combination with a pair distribution function (PDF) analysis. The results reveal that only an amorphous $LiNbO_3$ coating with a calcination temperature of 350 °C significantly improves the electrochemical performance of the CAM. In contrast, at higher calcination temperatures the coating crystallizes, while at lower calcination temperatures the coating becomes a mixed niobium oxide phase, both of which correlate with reduced battery performance.

1. Introduction

With the ever-increasing demand for energy storage, battery research is focusing on a wide range of options to further improve lithium-ion batteries. In particular, the incorporation of solid electrolytes (SE) has attracted considerable attention. Such solid-state batteries (SSBs) are expected to be superior in terms of increased energy and power density as well as safety.[1–3] To achieve higher energy densities research focuses on the usage of lithium transition metal oxides like $LiNi_{1-x-y}Co_xMn_yO_2$ (NCM) as cathode active material (CAM) in combination with thiophosphate-based SE, which have a high ionic conductivity of $\approx 10^{-3}$ S cm^{-1}.[4–6]

One key challenge in enhancing the performance of these batteries is minimizing degradation at the cathode/electrolyte interface.[7–9] Due to oxidation of the SE during charging, the formation of a highly resistive layer has been commonly observed. Additionally, the CAM loses contact with the SE and can therefore not participate in the electrochemical processes anymore.[7] Ultimately the combination of these two mechanisms leads to a steady decrease of the capacity over the lifetime of the SSB.

To circumvent these challenges, a protective coating layer can be applied on the surface of the NCM particles.[10–13] Materials used for such a protective coating should be chemically stable against the electrolyte as well as the CAM. Furthermore, they should be electron-insulating and highly Li-ion conductive.[12] Hence, despite the great relevance of these coatings their exact nature as processed often remains unclear due to their challenging structural characterization.[12,14] The usage of macroscopic techniques like X-ray diffraction for structural and chemical analysis is often difficult due to low amount of these nanometer thick coatings. In contrast, scanning transmission electron microscopy (STEM) in combination with energy dispersive X-ray spectroscopy (EDS) and electron energy loss spectroscopy (EELS), with a small probe diameter in the (sub-) Angstrom-range, is well suited for spectroscopic and structural analysis of these coatings.

In this work, we investigate the structure of the well-established coating material $LiNbO_3$, which is already also used

J. Haust, J. Belz, S. Ahmed, N. Adeli, F. Hüppe, K. Volz
mar.quest
Marburg Center for Quantum Materials and Sustainable Technologies
Philipps-University Marburg
D-35032 Marburg, Germany
E-mail: kerstin.volz@physik.uni-marburg.de

J. Haust, J. Belz, S. Ahmed, N. Adeli, F. Hüppe, K. Volz
Department of Physics
Philipps-University Marburg
Hans-Meerwein-Straße 6, D-35032 Marburg, Germany

Y. Guo, V. Mereacre, A.-L. Hansen, H. Ehrenberg, J. R. Binder
Institute for Applied Materials
Karlsruher Institute of Technology
Hermann-von-Helmholtz-Platz 1, D-76344 Eggenstein-Leopoldshafen, Germany

L. C. Erhard, J. Rohrer, K. Albe
Institute of Materials Science
Technical University of Darmstadt
Otto-Berndt-Strasse 3, D-64287 Darmstadt, Germany

The ORCID identification number(s) for the author(s) of this article can be found under https://doi.org/10.1002/admi.202500590

DOI: 10.1002/admi.202500590

for liquid electrolyte batteries.[15] Ionic Conductors like $LiNbO_3$ are expected to enhance charge transfer at the cathode–electrolyte interface, thereby improving electrochemical performance—particularly under high C-rate conditions. In addition, ceramic-based solid electrolyte coatings act as a physical barrier between the cathode and the electrolyte, effectively suppressing undesirable side reactions.[16]

$LiNbO_3$ is a promising material due to its high ion conductivity of 10^{-5}–10^{-6} S cm^{-1} in its amorphous phase.[12,14,15,17] The ion conductivity of the latter is several orders of magnitude higher than that of crystalline $LiNbO_3$, which highlights the importance of microscopic structural investigations.[18–20]

In the past, the crystallinity of the coating has been indirectly controlled through the synthesis temperature since the reported crystallization temperature for $LiNbO_3$ is in the range of 400–500 °C depending on the exact synthesis conditions.[18,21–23]

While bulk and thin-film chemistries may appear identical in certain cases, it cannot be assumed that interfacial chemistry and the effects of drastically reduced dimensionality follow the same trends observed in bulk materials. A general example of such deviations is the reported reduction in melting points of gold nanoparticles, as reported by Widemann et al.[24]

Given the nanoscale thickness of the coating, conventional X-ray diffraction often lacks the sensitivity required to resolve its structural characteristics. This limitation underscores the importance of STEM-based techniques, which can provide high-quality diffraction, analytical data, as well as imaging data from even nanometer scales.

For direct determination of the structure of the coating an advanced STEM technique, scanning precession electron diffraction (SPED), is utilized.[25–27] This technique is based on a precessed nanometer-sized probe with a small semi-convergence angle that is scanned across the sample to achieve high-quality pseudo-kinematic diffraction data for every scan point, resulting in the acquisition of a 4D data set. From this electron diffraction (ED) data so-called (reduced) pair distribution functions (rPDFs) are calculated to get insights into the structure of the sample.[28–33] These experimental rPDFs are compared with theoretical models to obtain the atomic arrangements in the amorphous structure of the coating.

To understand the influence of the structure of the coating on the electrochemical performance of the batteries, three coated NCM622 (60% Ni, 20% Co, and 20% Mn) samples calcinated at 550, 350, and 80 °C were compared, respectively. The samples are further referred to as *S550*, *S350*, and *S80*, corresponding to their respective calcination temperatures.

2. Results and Discussion

To determine the impact of the calcination temperature on the electrochemical properties, specific capacity measurements were conducted during the cycling of different battery cells. These utilized uncoated NCM622 as well as NCM622 coated at different calcination temperatures as CAM. In **Figure 1** the results of these experiments are shown. The four battery cells exhibit distinct differences during the measurement. At the beginning of the cycling, the battery cell with the uncoated CAM demonstrates the highest specific capacity, which then decreases continuously with each cycle. For *S80*, the battery cell with the coated CAM calcinated at the lowest temperature, the specific capacity drops almost to zero after around 5 cycles. *S350* and *S550* show an initial increase in specific capacity over the first 60 to 70 cycles, followed by a steady decline. This decline is less pronounced for *S350*, which also maintains a higher overall specific capacity compared to the other cells. After around 200 cycles this cell exhibits therefore a higher specific capacity than the cell with the uncoated CAM. These results suggest that a calcination temperature of ≈350 °C for the coated NCM enhances the electrochemical performance, making it the optimal temperature for improving the performance of the coated CAM in battery cells.

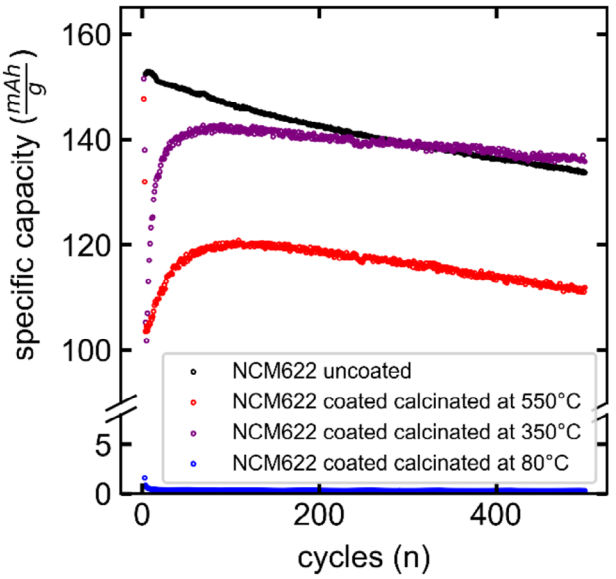

Figure 1. Specific capacity evolution cycled battery cells with uncoated NCM (black) and the coated samples S550 (red), S350 (purple), and S80 (blue).

To understand why only a calcination temperature of 350 °C leads to an improvement in the electrochemical performance, while the two other calcination temperatures lead to a coating, which results in a deterioration of the cell properties, the structure of all three coatings is investigated by TEM. For these investigations, NCM particles with thicker coatings were used to more effectively distinguish between the diffraction signals from the particle and the coating. A combination of protective deposition layers, including carbon, platinum, and tungsten, is applied to the particle surfaces during TEM sample preparation to ensure that the coating remains intact during the preparation process.

Initial insights into the morphological differences among these three samples are provided by the STEM EDS measurements shown in **Figure 2**.

For *S550* and *S350*, the coating forms a homogeneous film around the NCM particle as depicted in Figure 2a,b. To highlight the homogeneity of the coating, Figure S1 (Supporting Information) presents scanning electron microscopy (SEM) backscattered electron images of various focused ion beam (FIB) cross-sections of the coated NCM particles. Assuming a surface area of 0.26 m^{2}g^{-1} for NCM and a theoretical density of crystalline $LiNbO_3$ of 4.64 g cm^{-3}, the average thickness of the coating layer for the 6 wt.% $LiNbO_3$-coated NCM622 particles can be estimated

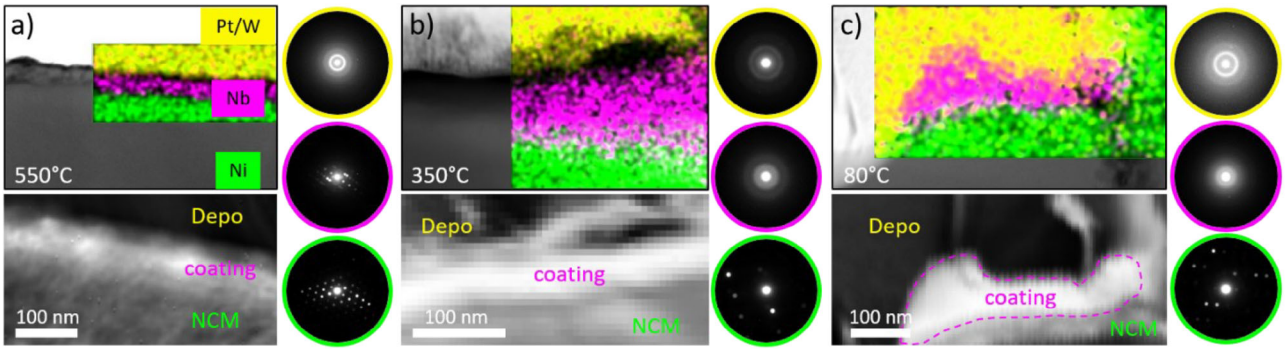

Figure 2. Electron microscopy data for the samples a) S550, b) S350, and c) S80, respectively. (Top row) STEM high-angle annular dark field (HAADF) images for each sample with EDS maps as insets. (Bottom row) Virtual annular dark field (VADF) images (angular range, 12–24 mrad) from SPED 4D-datasets for the respective sample. Next to the images of the respective samples, averaged diffraction patterns from the SPED 4D-datasets for the NCM particle (green), coating (magenta), and protective layer depositions (Pt/W) (yellow) are shown. The diffraction patterns show the crystalline structure of the $LiNbO_3$ coating in the case of S550 and the amorphous structure of the coating for S350 and S80, respectively.

at ≈50 nm.[34] This estimation is consistent with the values observed in the STEM-HAADF images shown in Figure 2a,b. In the case of *S80*, the coating covers only selective areas of the particle surface, exemplarily shown in Figure 2c. This observation underscores the need for a higher calcination temperature to achieve more uniform coverage of the NCM particles.

In addition to the morphological analysis, the niobium-to-oxygen ratio in the coating areas can be estimated through the STEM EDS measurements.

For all three samples, the Nb, O ratio is consistent with the expected stoichiometry of $LiNbO_3$, ≈1, 3. However, the Nb/O ratio derived from STEM-EDS measurements is significantly influenced by the signal quality of both elemental peaks. In this specific measurement geometry, both Nb and O signals suffer from a generally low signal-to-noise ratio. This is primarily due to substantial X-ray absorption in the EDS window for low-energy photons, compounded by peak overlaps involving Nb, W, and Pt—elements commonly present due to standard FIB lamella preparation, where W or Pt is used as protective deposition layers.

Additionally, the EDS spectra do not show an increased amount of C in the samples calcinated at lower temperature. The negligible carbon peaks depicted in Figure S5 (Supporting Information) are within the typical regime of preparation and measurement-induced spurious carbon contamination.

This result does not yet account for the differences in electrochemical performance observed among the samples. Two key questions remain unresolved, First, what accounts for the differing electrochemical properties of *S350* and *S550*, despite both having a homogeneous coating around the NCM particles? Second, why does the inhomogeneous coating on *S80*, characterized by incomplete coverage, lead to a complete failure of the corresponding battery cell?

To answer these two questions, SPED 4D datasets are recorded to investigate the structure of the coating. Through this, localized structural information of the sample is obtained. In addition, SPED, with its electron beam size of only a few nanometers, is ideally suited for the structural investigation of such thin coatings.

Virtual annular dark field images (VADF) derived from these datasets, shown in Figure 2, provide an overview of the scanned area. Using an angular collection range of 12–24 mrad for these VADF images, the coating appears as a bright layer on top of the NCM particle. This contrast difference allows the identification of the different layers and subsequently the averaging of the diffraction patterns over the respective regions. These position-averaged electron diffraction patterns (PAED) are also shown in Figure 2 encircled with different colors to clarify their origin.

For *S550*, the PAED for the coating (magenta) in Figure 2a shows a spot-like diffraction pattern, indicating a polycrystalline structure of the coating. The comparison of this PAED image with the one for the NCM particle, also depicted in Figure 2a (green), reveals that the coating has a different crystalline structure than the NCM particle. In the case of *S350* and *S80*, the PEAD images for the coatings shown in Figure 2b,c reveal broad diffuse rings, pointing to an amorphous structure of the coating at lower calcination temperatures.

These findings demonstrate that $LiNbO_3$, when applied as a thin film coating on NCM, exhibits a crystallization temperature between 350 and 550 °C, which is consistent with previously reported values for bulk $LiNbO_3$.[21,23,35] This helps address the first question regarding the differences in electrochemical performance mentioned earlier. Amorphous $LiNbO_3$ is known for having a higher ionic conductivity than its crystalline counterpart.[18–21] Thus, this could explain why *S350*, with its amorphous coating, exhibits better electrochemical performance compared to *S550*, which features a crystalline coating, despite both samples having a homogeneous coating around the NCM particles.

What remains to be explained is the poor electrochemical performance of a battery cell with a coated CAM calcined at 80 °C. If its amorphous coating exhibited similar electrochemical properties to the amorphous coating obtained at the 350 °C calcination temperature, even an inhomogeneous coating—covering only parts of the NCM particle—should still improve the electrochemical performance of the respective battery cell compared to one with an uncoated CAM.[36] In contrast, the nearly complete failure of the battery cell with the coated CAM calcined at 80 °C suggests a significant difference in the nature of the two amorphous coatings calcined at 350 and 80 °C.

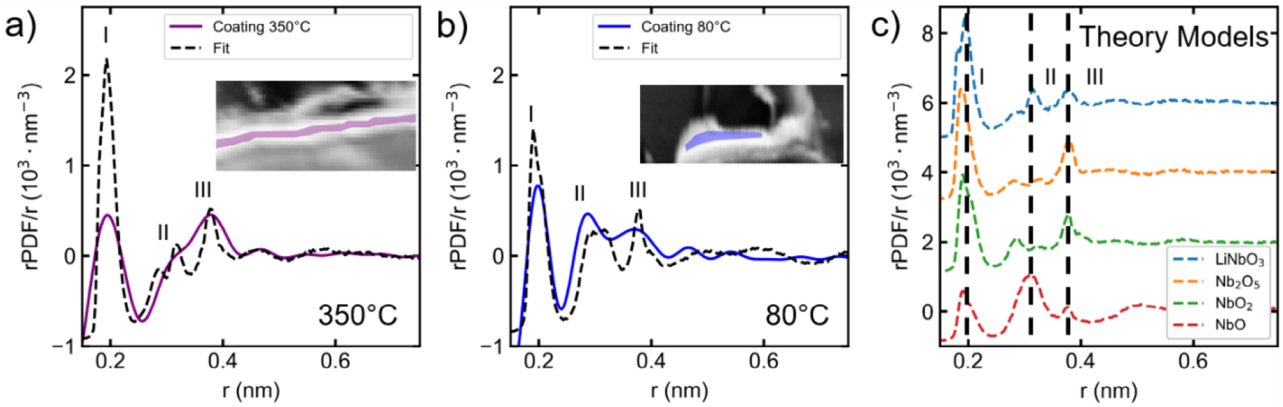

Figure 3. rPDFs (purple and blue) calculated from the amorphous diffraction of the coating in the SPED 4D- datasets shown in Figure 2, for S350 a) and S80 b), respectively. Fitting a weighted mean (dashed black) from simulated rPDFs c) for $LiNbO_3$ and different niobium oxides to the experimental data gives an estimation for the coating about being a more $LiNbO_3$- or Niobium oxide-rich phase.

To address this, further investigation of the amorphous structures of the coatings of *S350* and *S80* is required. This can be achieved by deriving the rPDFs for the coating layers, based on the amorphous diffraction patterns shown in Figure 2b,c. The rPDF is obtained by Fourier transforming the background-corrected radial-averaged diffraction. It resembles a histogram with peaks corresponding to frequently occurring atomic distances, known as correlation distances within the sample.[29,30] These plots can therefore be utilized to analyze the structure-property relationships of various coatings.

Figure 3a,b shows these experimental rPDFs for the coating of *S350* and *S80* in purple and blue, respectively, alongside the simulated rPDFs (black dashed curves, discussed below). In the case of *S350*, the experimental rPDF (Figure 3a) has three prominent peaks at 0.20, 0.32, and 0.37 nm correlation distance. These peaks are labeled as peak I, peak II, and peak III, as illustrated in Figure 3. For *S80*, the experimental rPDF, depicted in Figure 3b, also shows these three peaks, but with two notable differences in the characteristics of peak II and peak III. First, peak II shifts to a lower correlation distance of 0.29 nm for *S80*. Additionally, in contrast to *S350*, peak II is more pronounced than peak III for *S80*, indicating a higher coordination number and with that a higher ratio of atom pairs with this correlation distance. These differences in the rPDFs for the coating in the two samples point to a different amorphous structure of the coating depending on the calcination temperature.

One possible explanation for this, as suggested in X-ray diffraction studies of $LiNbO_3$ thin films synthesized from aqueous Nb-polyoxometalates by Nyman et al., is that, depending on the synthesis conditions, the coating may not consist of pure $LiNbO_3$ but rather be a mixture of $LiNbO_3$ and various niobium oxide phases.[37] To explore this, the experimental results are compared with simulated amorphous model structures for $LiNbO_3$, as well as the known stable niobium oxides Nb_2O_5, NbO_2, and NbO.[38,39]

Figure 3c shows the rPDFs for these four model structures. The partial rPDFs for the O—O, the Nb—O, and the Nb–Nb correlations are shown in Figure S1 (Supporting Information). These partial rPDFs explain the positions of peak I–III. For all four compounds, peak I is associated with the Nb—O bonding distance of 0.20 nm, while peak III corresponds to the second-order Nb—Nb correlation distance at 0.37 nm. Peak II represents the O—O or Nb—Nb correlation distances, observed at 0.29 and 0.32 nm, respectively. As shown in Figure S1 (Supporting Information) both of these peaks are more pronounced in niobium oxides compared to $LiNbO_3$. This suggests that the shift of peak II from 0.32 nm in the rPDF of *S350* to 0.29 nm in the rPDF of *S80* reflects a change in the nature of the coating; in *S350* its structure is more influenced by $LiNbO_3$, while in *S80*, it is predominantly governed by niobium oxides.

This is supported by fitting a weighted mean of the rPDFs for these four model systems to the experimental data for *S350* and *S80*, to estimate the ratios of the different phases in the coating. The fits with the minimal squared difference to the respective experimental data are shown as black dashed curves in Figure 3a,b. The fit for *S350* primarily consists of rPDFs of $LiNbO_3$, whereas for *S80*, the fit shifts toward a higher proportion of niobium oxides. It again indicates a greater presence of niobium oxides in the coating of the sample calcined at the lower temperature.

Our approach of capturing a nanometer-resolved 4D dataset and extracting relevant diffraction data from specific regions within the sample offers the advantage of spatially resolving structural variations. This enables us to examine the diffraction at the interface between the coating and the NCM particle, thereby elucidating the influence of the particle surface on the synthesis and structural characteristics of the coating.

While the amorphous structure of the coating depends on the calcination temperature for the main bulk regions several nanometers away from the coating/NCM interface, this does not appear to be the case for the structure of the coating directly at the coating/NCM interface. **Figure** 4 presents the rPDFs for the coating in *S350* and *S80*, calculated from the diffraction at the coating/NCM interface (see inset). The similarity between the two curves suggests that the coating structure close to the interface is comparable for both calcination temperatures. This is further supported by the comparison of the pair distribution functions (PDFs) of the coatings from samples *S350* and *S80*, as well as by comparing the PDFs of the coating and the interface regions within each sample, as shown in Figure S3 (Supporting Information). One possible explanation for this similarity is that the interface structure is predominantly governed by

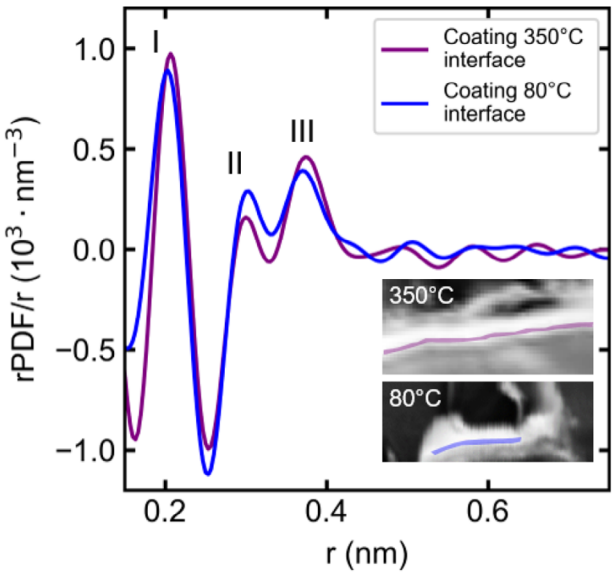

Figure 4. The rPDF calculated from the amorphous diffraction of the $LiNbO_3$ coating in S350 (purple) and S80 (blue) of scan points close to the coating/NCM interface, as depicted in the insets.

the interaction between the coating and NCM. This is supported by comparing the position at peak I in the rPDFs of the coating, shown in Figure 3a,b, with the position of peak I in the rPDFs for the interfaces, depicted in Figure 4. While the position of peak I is at 0.20 nm in the case of the coating it shifts in the rPDFs for the interfaces to 0.21 nm. As discussed above the rPDF of the coating peak I is associated with the Nb—O bond length in $LiNbO_3$ and niobium oxides. The slightly larger value observed at the interface is consistent with values reported for the Nb—O bond length in Li_3NbO_4-like compounds.[40–42] The similarity in the interface structure, despite the distinct characteristics of the coatings calcined at 350 and 80 °C, emphasizes the key role of the NCM surface in the formation of the coating. This changes after several nm of coating. When the surface of the NCM is not anymore active the rest of the coating forms probably due to the starting materials at low calcination temperatures a mixture of niobium oxides or even niobium hydroxides. This layer, exhibiting a low or negligible ionic conductivity, leads to an inadequate contact between the active material and the electrolyte, thereby compromising the electrochemical performance of the respective battery cell. At higher temperatures the oxides/hydroxides react with each other resulting in an amorphous $LiNbO_3$ compound with better electrochemical properties leading to a superior electrochemical performance in the respective battery cell with the coated CAM calcined at 350 °C temperatures.

3. Conclusion

By combining SPED with an rPDF analysis and theoretical modeling, we identify a direct link between the structure of different coatings on NCM and the electrochemical performance when utilizing the respective coated CAM in a battery cell. The structure of the thin film coatings is for the first few nm dominated by the influence of the NCM surface. After that, it is dependent on the calcination temperature in the synthesis process. Only a calcination temperature of ≈350 °C leads to an improvement in the electrochemical performance of the NCM utilized as CAM in a battery cell compared to uncoated NCM. At a calcination temperature of 550 °C, the coating forms a homogeneous conformal film on the NCM surface having a crystalline structure. This seems to negatively affect the conductivity of the coating. While the overall morphology remains similar, the structure becomes amorphous for the coating calcined at 350 °C, which, due to the higher ionic conductivity of amorphous $LiNbO_3$, explains the enhanced electrochemical performance. A lower calcination temperature of 80 °C results in a different amorphous structure, likely caused by a transition from a $LiNbO_3$-rich phase coating to a mixture dominated by niobium oxides/hydroxides, most likely due to the calcination temperature being insufficient to fully react the coating precursors, which in turn significantly degrades the ionic conductivity. Consequently, the battery cell with the CAM coated at 80 °C exhibits the poorest electrochemical performance.

4. Experimental Section

Electron Microscopy—Sample Preparation: TEM lamellae are prepared using JEOL JIB-4601F focused ion beam (FIB) and Helios 5 Hydra CX plasma-FIB systems. Prior to FIB processing, the samples were sputter-coated with a thin carbon layer approximately a few tens of nanometers thick, followed by a platinum coating of ≈150–200 nm using the EM ACE600 Sputter-Coater from Leica. Subsequently, the sample surfaces were coated with a tungsten layer, with a thickness of 3–4 µm, applied using either Ga-ion or Xe-ion beams depending on the specific FIB instrument employed. The coated particles were then mounted onto a TEM grid using micromanipulator needles and initially milled to a thickness of ≈300–250 nm using 30 kV Ga-ion or Xe-ion beams. Final polishing was performed using 5 kV ion beams, reducing the sample thickness to below 100 nm.

Electron Microscopy—STEM EDS: The STEM EDS measurements were performed at an aberration-corrected JEOL JEM-2200 (Scanning) Transmission Electron Microscope operating at 200 kV and equipped with a Bruker XFlash 5060 EDS detector. For data evaluation and visualization, the Bruker Esprit 1.9 software was used.

Electron Microscopy—SPED: SPED measurements were performed at a JEOL JEM-3010 operating at 300 kV. Scanning and precessing the electron beam with an angle of 0.6° was done by a NanoMEGAS P2010 system. The images during the scan are acquired as a data stream with a sensitive and fast TVIPS X416F-ES 4K camera and are afterward converted and processed using Python code, where the individual diffraction patterns are assigned by their timestamps to a position in the 2D scan grid. Extracting the PDF from the electron diffraction data was done following an adapted method from Tran et al.[28,31,32]

Theoretical Modeling: The amorphous structure models were generated by melt-quench simulations using a machine-learning interatomic potential based on the nonlinear atomic cluster expansion.[43–45] For the melt-quench simulations, the same protocol was used as in,[46] but with component-adjusted maximum temperatures. The protocol started from crystalline configurations and randomize these at high temperatures ($LiNbO_3$, NbO_2 and Nb_2O_5, 2500 K, NbO, 3500 K) under an NVT ensemble for 10 ps. Then it immediately lowered the temperature by 500 K and equilibrated the structures under an NPT ensemble at zero external pressure for 100 ps. Finally, it quenched the structures to room temperature at a quenching rate of 1012 K s^{-1}. Molecular dynamics simulations were performed using LAMMPS.[47] A time step of 1 fs, a temperature damping parameter of 100 fs, and a pressure damping parameter of 1000 fs were used The PDFs for the models were calculated using scripts provided in previous work[48] based on the ovito python package.[49]

The database for the potential was based on crystalline structures extracted from the Materials Project database,[42] and was then

systematically extended by active learning. Lithium oxidates, niobium oxides, and lithium niobates were included with different stoichiometries. From these crystalline phases, active learning was started within molecular dynamics simulations using the following protocol, it was started by equilibrating at 200 K for 10 ps, followed by annealing to 2000 K for 200 ps and cooling to 200 K for another 200 ps. This entire process was performed under NPT conditions. Uncertainty reporting was used based on the D-optimality criterion as implemented for ACE[50] with an extrapolation grade of 5 for adding structures to the database, and 25 for stopping the simulation. In later iterations, the maximum temperature was increased to 3500 K and a maximum volume of 40 $Å^3$ per atom as a stopping criterion was added. In these later iterations also structures with carbon were added to the database, for example in the form of lithium and niobium carbides with different chemical ratios and lithium carbonate. For the density functional theory single point evaluations, GPAW was used[51] with the PBE exchange correlation functional,[52] a plane wave energy cutoff of 800 eV, a k-point density of 3.5 $Å^{-1}$ and a stopping criterion of the electronic self-consistency cycle of 0.001 eV $Å^{-1}$.

Synthesis: For the coating solution 0.93 g niobium(V) ethoxide and 0.17 g lithium ethoxide were dissolved in 60 and 120 mL absolute ethanol, respectively. The solutions were combined, followed by the addition of 180 mL of hydrogen peroxide (30%) and 0.3 mL nitric acid (HNO_3, 65%) to obtain a clear solution.

To coat NCM622 (Single Crystal (MSE Supplies)) with ≈6% $LiNbO_3$ (or 0.5% $LiNbO_3$) 3 g of NMC622(SC) and 30 mL absolute ethanol were added into a round bottom flask. The obtained solution was stirred for ≈3 min and 155 mL (or 13 mL) of the coating solution was added dropwise under continuous stirring. The mixture was stirred until no more gas elimination was observed (24 h). The suspension was then decanted and the powder was washed with ethanol, centrifuged, dried at 80 °C, and calcined in air, first at 250 °C for 2 h and at target temperatures (350 and 550 °C) for 5 h with heating and cooling rate of 4 K min^{-1}. The coated material was stored in a glovebox.

Electrochemistry: The electrochemistry for the materials coated with 0.5% $LiNbO_3$ was done as previously reported.[53] For the preparation of electrodes, the slurry consisted of 80 wt.% active material, 10 wt.% Super-C carbon black and 10 wt.% PVDF with NMP (1-Methyl-2-pyrrolidinone) as solvent was used. For the cell assembly, 2032 coin cells were used. The electrolyte was 1.0 M LiPF6 solution in 1, 1 v/v ethylene carbonate, diethyl carbonate (EC, DEC) and a lithium metal foil (diameter 12 mm, thickness 25 µm) was used as anode. Celgard 2325 (Celgard, Sélestat, France) was used as separator. Cycling performance was performed at a charge rate of C/2 and discharge rate of 1 C. Cycling was performed at a temperature of 22 °C and a voltage window of 3.0–4.3V vs Li^+/Li was applied.

Supporting Information

Supporting Information is available from the Wiley Online Library or from the author.

Acknowledgements

Funding from the European Regional Development Fund (ERDF) and the Recovery Assistance for Cohesion and the Territories of Europe (REACT-EU), as well as the Bundesministerium für Bildung und Forschung (BMBF) within the FESTBATT cluster of competence (projects 03XP0433D, 03XP0435C, and 03XP0433A) is gratefully acknowledged. We also acknowledge the support of the German Research Foundation (DFG) via INST 160/724-1FUGG. The authors gratefully acknowledge the computing time provided on the high-performance computer Lichtenberg II at TU Darmstadt, funded by the German Federal Ministry of Education and Research (BMBF), and the State of Hesse Ministry of Science and Research, Art and Culture (HMWK).

Conflict of Interest

The authors declare no conflict of interest.

Data Availability Statement

The data that support the findings of this study are available from the corresponding author upon reasonable request.

Keywords

4D-STEM, amorphous materials, coating, ePDF, interfaces, PED, SSB

Received: June 26, 2025
Published online: August 14, 2025

[1] J. Schnell, T. Günther, T. Knoche, C. Vieider, L. Köhler, A. Just, M. Keller, S. Passerini, G. Reinhart, *J. Power Sources* **2018**, *382*, 160.
[2] T. Schmaltz, F. Hartmann, T. Wicke, L. Weymann, C. Neef, J. Janek, *Adv. Energy Mater.* **2023**, *13*, 2301886.
[3] J. Janek, W. G. Zeier, *Nat. Energy* **2016**, *1*, 1.
[4] N. Kamaya, K. Homma, Y. Yamakawa, M. Hirayama, R. Kanno, M. Yonemura, T. Kamiyama, Y. Kato, S. Hama, K. Kawamoto, A. Mitsui, *Nat. Mater.* **2011**, *10*, 682.
[5] D. Kitsche, Y. Tang, Y. Ma, D. Goonetilleke, J. Sann, F. Walther, M. Bianchini, J. Janek, T. Brezesinski, *ACS Appl. Energy Mater.* **2021**, *4*, 7338.
[6] Y. Kato, S. Hori, T. Saito, K. Suzuki, M. Hirayama, A. Mitsui, M. Yonemura, H. Iba, R. Kanno, *Nat. Energy* **2016**, *1*, 1.
[7] R. Koerver, I. Aygün, T. Leichtweiß, C. Dietrich, W. Zhang, J. O. Binder, P. Hartmann, W. G. Zeier, J. Janek, *Chem. Mater.* **2017**, *29*, 5574.
[8] J. Zheng, S. Myeong, W. Cho, P. Yan, J. Xiao, C. Wang, J. Cho, J.-G. Zhang, *Adv. Energy Mater.* **2017**, *7*, 1601284.
[9] P. K. Nayak, E. M. Erickson, F. Schipper, T. R. Penki, N. Munichandraiah, P. Adelhelm, H. Sclar, F. Amalraj, B. Markovsky, D. Aurbach, *Adv. Energy Mater.* **2018**, *8*, 1702397.
[10] D. Weber, Đ. Tripković, K. Kretschmer, M. Bianchini, T. Brezesinski, *Eur. J. Inorg. Chem.* **2020**, *2020*, 3117.
[11] A. Kim, F. Strauss, T. Bartsch, J. H. Teo, T. Hatsukade, A. Mazilkin, J. Janek, P. Hartmann, T. Brezesinski, *Chem. Mater.* **2019**, *31*, 9664.
[12] S. P. Culver, R. Koerver, W. G. Zeier, J. Janek, *Adv. Energy Mater.* **2019**, *9*, 1900626.
[13] X. Bai, F. Xie, Z. Zhang, M. Cao, Q. Wang, S. Wang, C. Liu, X. Su, Z. Lin, G. Cui, *Adv. Energy Mater.* **2024**, *14*, 2401336.
[14] F. Walther, F. Strauss, X. Wu, B. Mogwitz, J. Hertle, J. Sann, M. Rohnke, T. Brezesinski, J. Janek, *Chem. Mater.* **2021**, *33*, 2110.
[15] G. Hu, Y. Tao, Y. Lu, J. Fan, L. Li, J. Xia, Y. Huang, Z. Zhang, H. Su, Y. Cao, *ChemElectroChem* **2019**, *6*, 4773.
[16] U. Nisar, N. Muralidharan, R. Essehli, R. Amin, I. Belharouak, *Energy Storage Mater.* **2021**, *38*, 309.
[17] B. N. Nunes, W. van den Bergh, F. Strauss, A. Kondrakov, J. Janek, T. Brezesinski, *Inorg. Chem. Front.* **2023**, *10*, 7126.
[18] Y. Ito, I. Tsuyumoto, *Mater. Chem. Phys.* **2021**, *272*, 125035.
[19] A. V. Yatsenko, S. V. Yevdokimov, A. A. Yatsenko, *Ferroelectrics* **2021**, *576*, 157.
[20] A. V. Yatsenko, M. N. Palatnikov, N. V. Sidorov, A. S. Pritulenko, S. V. Evdokimov, *Phys. Solid State* **2015**, *57*, 1547.
[21] A. M. Glass, K. Nassau, T. J. Negran, *J. Appl. Phys.* **1978**, *49*, 4808.
[22] P. Heitjans, M. Masoud, A. Feldhoff, M. Wilkening, *Faraday Discuss.* **2007**, *134*, 67.
[23] S. Hirang, T. Yogo, K. Kikuta, Y. Isobe, S. Ono, *J. Mater. Sci.* **1993**, *28*, 4188.
[24] M. Widemann, D. Krug, O. Maßmeyer, F. Gruber, A. Beyer, K. Volz, *Small Methods* **2024**, *8*, 2301079.
[25] P. P. Das, S. Nicolopoulos, M. Gemmi, *Acta Crystallogr., Sect. A: Found. Crystallogr.* **2017**, *73*, C983.

[26] Y. Chou, K. B. Borisenko, P. P. Das, S. Nicolopoulos, M. Gemmi, A. I. Kirkland, *Symmetry* **2023**, *15*, 1291.
[27] A. Avilov, K. Kuligin, S. Nicolopoulos, M. Nickolskiy, K. Boulahya, J. Portillo, G. Lepeshov, B. Sobolev, J. P. Collette, N. Martin, A. C. Robins, P. Fischione, *Ultramicroscopy* **2007**, *107*, 431.
[28] J. Belz, J. Haust, M. J. Müller, K. Eberheim, S. Schwan, S. Gowrisankar, F. Hüppe, A. Beyer, P. R. Schreiner, D. Mollenhauer, S. Sanna, S. Chatterjee, K. Volz, *J. Phys. Chem. C* **2022**, *126*, 9843.
[29] D. J. Cockayne, *Annu. Rev. Mater. Res.* **2007**, *37*, 159.
[30] K. M. Ehrhardt, R. C. Radomsky, S. C. Warren, *Chem. Mater.* **2021**, *33*, 8990.
[31] J. Haust, J. Belz, M. Müller, B. K. Danilo, J. Link Vasco, F. Hüppe, I. Rojas Léon, J. Christmann, A. Beyer, S. Dehnen, N. W. Rosemann, W.-C. Pilgrim, S. Chatterjee, K. Volz, *ChemPhotoChem* **2022**, *6*, 202200071.
[32] D. T. Tran, G. Svensson, C. Tai, *J. Appl. Crystallogr.* **2017**, *50*, 304.
[33] N. Yang, C. Ophus, B. H. Savitzky, M. C. Scott, K. Bustillo, K. Lu, *Mater. Charact.* **2021**, *181*, 111512.
[34] P. Stüble, V. Mereacre, H. Geßwein, J. R. Binder, *Adv. Energy Mater.* **2023**, *13*, 2203778.
[35] N. Özer, C. M. Lampert, *Sol. Energy Mater. Sol. Cells* **1995**, *39*, 367.
[36] W. S. K. Bong, A. Shiota, T. Miwa, Y. Morino, S. Kanada, K. Kawamoto, *J. Power Sources* **2023**, *577*, 233259.
[37] T. Rahman, N. Martin, J. Jenkins, R. Elzein, D. Fast, R. Addou, G. S. Herman, M. Nyman, *Inorg. Chem.* **2022**, *61*, 3586.
[38] T. Yi, H. M. K. Sari, X. Li, F. Wang, Y. Zhu, J. Hu, J. Zhang, X. Li, *Nano Energy* **2021**, *85*, 105955.
[39] C. Nico, T. Monteiro, M. Graça, *Prog. Mater. Sci.* **2016**, *80*, 1.
[40] K. Ukei, H. Suzuki, T. Shishido, T. Fukuda, *Cryst. Struct. Commun.* **1994**, *50*, 655.
[41] Materials Data on Li3NbO4 by Materials Project: LBNL Materials Project; Lawrence Berkeley National Laboratory (LBNL), Berkeley, CA, USA **2020**.
[42] A. Jain, S. P. Ong, G. Hautier, W. Chen, W. D. Richards, S. Dacek, S. Cholia, D. Gunter, D. Skinner, G. Ceder, K. A. Persson, *APL Mater.* **2013**, *1*, 1.
[43] A. Bochkarev, Y. Lysogorskiy, S. Menon, M. Qamar, M. Mrovec, R. Drautz, *Phys. Rev. Materials* **2022**, *6*, 013804.
[44] R. Drautz, *Phys. Rev. B* **2019**, *99*, 249901.
[45] Y. Lysogorskiy, C. van der Oord, A. Bochkarev, S. Menon, M. Rinaldi, T. Hammerschmidt, M. Mrovec, A. Thompson, G. Csányi, C. Ortner, R. Drautz, *npj Comput Mater.* **2021**, *7*, 97.
[46] L. C. Erhard, J. Rohrer, K. Albe, V. L. Deringer, *npj Comput. Mater.* **2022**, *8*, 90.
[47] A. P. Thompson, H. M. Aktulga, R. Berger, D. S. Bolintineanu, W. M. Brown, P. S. Crozier, P. J. in 't Veld, A. Kohlmeyer, S .G. Moore, T. D. Nguyen, R. Shan, M. J. Stevens, J. Tranchida, C. Trott, S. J. Plimpton, *Comput. Phys. Commun.* **2022**, *271*, 108171.
[48] L. C. Erhard, J. Rohrer, K. Albe, V. L. Deringer, *Nat. Commun.* **2024**, *15*, 1927.
[49] A. Stukowski, *Modelling Simul. Mater. Sci. Eng.* **2010**, *18*, 15012.
[50] Y. Lysogorskiy, A. Bochkarev, M. Mrovec, R. Drautz, *Phys. Rev. Materials* **2023**, *7*, 043801.
[51] J. J. Mortensen, A. H. Larsen, M. Kuisma, A. V. Ivanov, A. Taghizadeh, A. Peterson, A. Haldar, A. O. Dohn, C. Schäfer, E. Ö. Jónsson, E. D. Hermes, F. A. Nilsson, G. Kastlunger, G. Levi, H. Jónsson, H. Häkkinen, J. Fojt, J. Kangsabanik, J. Sødequist, J. Lehtomäki, J. Heske, J. Enkovaara, K. T. Winther, M. Dulak, M. M. Melander, M. Ovesen, M. Louhivuori, M. Walter, M. Gjerding, O. Lopez-Acevedo, et al., *J. Chem. Phys.* **2024**, *160*, 092503.
[52] J. P. Perdew, K. Burke, M. Ernzerhof, *Phys. Rev. Lett.* **1996**, *77*, 3865.
[53] V. Mereacre, P. Stüble, A. Ghamlouche, J. R. Binder, *Nanomaterials* **2021**, *11*, 548.